Evaluating Ground Deformation in Low-Coherence Agricultural Areas Using Multi-Temporal InSAR Analysis

Mingyue Ma[1], Mahmud Haghshenas Haghighi[1], Mahdi Motagh[1,2]

[1] Institute of Photogrammetry and GeoInformation, Leibniz University Hannover, Germany - (mingyue.ma, mahmud)@ipi.uni-hannover.de
[2] GFZ Helmholtz Centre for Geosciences, Germany - mahdi.motagh@gfz.de

Keywords: Multi-Temporal InSAR, Ground deformation, Sentinel-1, Low-coherence agricultural areas, Golestan.

Abstract

Ground deformation caused by excessive groundwater extraction has become a major environmental concern in agricultural regions worldwide. Interferometric Synthetic Aperture Radar (InSAR) enables large-scale monitoring of ground deformation. However, its performance often decreases in low-coherence areas affected by vegetation growth and irrigation. In this study, we conducted a comparative evaluation of three multi-temporal SBAS-InSAR processing frameworks, MintPy, LiCSBAS, and SARvey, to assess their consistency in monitoring ground deformation across Golestan Province, Iran, using Sentinel-1 data acquired between 2014 and 2024. The analysis included deformation velocity fields, cross-sectional profiles, and time-series displacements, which were compared with temperature and precipitation variations. All three frameworks identified a pronounced deformation zone in the Gorgan Plain, with maximum line-of-sight deformation rates up to 13 cm/year. Quantitative comparisons showed strong correlations among the frameworks (r = 0.80 to 0.89), confirming their mutual reliability even under low coherence conditions. The time-series analysis revealed clear seasonal deformation patterns, with summer subsidence and winter uplift closely related to hydroclimatic fluctuations. Overall, this study demonstrates that multi-temporal SBAS-InSAR approaches can provide consistent and physically meaningful deformation estimates in challenging agricultural environments, offering valuable insights for subsidence monitoring and water resource management.

1. Introduction

Ground deformation is a globally prevalent geohazard that results from both natural processes and human activities such as groundwater extraction, excessive irrigation, and urban expansion. It poses significant risks to infrastructure stability, agricultural productivity, and long-term land usability. In areas with intensive land use and poor groundwater regulation, the impacts are often irreversible. For example, in California’s Central Valley, cumulative subsidence has exceeded 9 meters and caused damage to canals and roads (Faunt et al., 2016). In Mexico City, rates of more than 30 cm per year have been recorded during drought periods, leading to serious structural deformation (Osmanoğlu et al., 2011). In Jakarta, subsidence has increased exposure to coastal flooding, and the city has experienced 23 major floods in the past 40 years (Takagi et al., 2021).

Traditional geodetic techniques, such as leveling and GPS field surveys, can achieve high measurement accuracy. However, they require significant time, labor, and cost, which makes them unsuitable for monitoring ground deformation over large areas. InSAR is a satellite-based measurement method with frequent revisit cycles, large spatial coverage, and high accuracy, which enables continuous monitoring of surface displacement over time (Zebker and Goldstein, 1986; Bürgmann et al., 2000). Gabriel et al. (1989) first proposed the Differential InSAR (D-InSAR) technique. Since then, it has been widely applied to ground deformation studies related to earthquakes, landslides and groundwater extraction (Massonnet et al., 1993; Tarchi et al., 2003; Bawden et al., 2001). D-InSAR can capture surface displacement, but it is often affected by atmospheric delay and temporal or spatial decorrelation (Zebker et al., 1992). To overcome these limitations, time-series InSAR methods were developed. Among them, Persistent Scatterer InSAR (PS-InSAR) (Ferretti et al., 2002) and Small Baseline Subset InSAR (SBAS-InSAR) (Berardino et al., 2003) are the most widely used. PS-InSAR is well suited for urban areas with stable scatterers such as buildings and infrastructure. SBAS-InSAR is more effective in non-urban areas where moderate coherence is available. However, in heavily vegetated or agricultural regions, coherence loss due to seasonal vegetation growth, irrigation, and land-use change remains a key challenge.

Iran is among the countries most severely affected by land subsidence, owing to its arid to semi-arid climate, water-intensive agriculture, and growing urban demand. Groundwater resources meet over 55% of the nation’s total water needs, and this figure rises to more than 80% in rural communities (Maghrebi et al., 2021). Decades of overextraction have caused dramatic declines in groundwater tables and widespread aquifer compaction, leading to large-scale subsidence across many basins. InSAR techniques have been particularly effective in the Central Plateau of Iran, where dry climate and sparse vegetation ensure high coherence for stable, long-term deformation monitoring. Cities such as Tehran, Qom, Kashan, Varamin, and Rafsanjan have been widely studied, revealing well-defined subsidence zones with rates exceeding 20–30 cm/year (Motagh et al., 2017; Mohebbi Tafreshi et al., 2021; Mahmoudpour et al., 2016). However, regions like Golestan Province in the northeast present different challenges. High precipitation supports dense seasonal vegetation and intensive farming, causing significant temporal decorrelation and reduced phase stability. These conditions limit InSAR effectiveness and make it challenging to perform reliable InSAR analysis in the area. For example, Haghighi and Motagh (2024b) reported localized subsidence up to 12 cm/year, while Payne et al. (2025) masked the region entirely due to low coherence. This discrepancy underscores the need to evaluate InSAR performance in low-coherence environments like Golestan, especially when different processing pipelines produce divergent interpretations.

This contribution has been peer-reviewed. The double-blind peer-review was conducted on the basis of the full paper.
https://doi.org/10.5194/isprs-annals-XI-3-2026-433-2026

Several SBAS-based InSAR frameworks have been developed to monitor large-scale and long-term ground deformation such as MintPy, LiCSBAS, and SARvey (Yunjun et al., 2019; Morishita et al., 2020; Piter et al., 2024). They use unwrapped interferometric phases to calculate time-series deformation and reconstruct ground displacement over time. While all are grounded in the same theoretical principles, they differ in key algorithmic choices such as interferogram network construction, coherence thresholds, time-series inversion strategies, and reference pixel selection. These variations can influence the spatial coverage, and reliable estimation of deformation time-series. This impact is especially significant in challenging environments like Golestan, where temporal decorrelation and vegetation dynamics already limit signal quality. Previous studies (Haghighi and Motagh, 2024b; Payne et al., 2025) applying different methods to the same region have reported divergent outcomes, raising uncertainty not only about the underlying deformation but also about the robustness of the processing strategies themselves. Ideally, independent pipelines applied to the same data should converge toward consistent results, especially when the physical phenomenon being observed is slow and spatially continuous, as is often the case with land subsidence. In this context, a systematic comparison of these pipelines over Golestan is critical, not to determine which is correct, but to assess how well they agree when faced with low-coherence conditions.

In this study, we aim to evaluate the consistency and applicability of three SBAS-InSAR processing approaches, monitoring land subsidence in Golestan Province, Iran. This region presents unique challenges for InSAR-based deformation analysis due to extensive cropland, seasonal vegetation, and moderate coherence loss. By applying both ascending and descending Sentinel-1 datasets from 2014 to 2024, we assess the spatial agreement among different deformation products and compare them with results from previous studies. The analysis includes a comparison of velocity fields, deformation profiles, displacement time-series at selected points and relationship with temperature and precipitation. Through this multi-method evaluation, we seek to identify the strengths and limitations of each processing pipeline in low-coherence environments and contribute to improving the reliability of InSAR-based monitoring in agricultural regions.

2. Study Area and Data

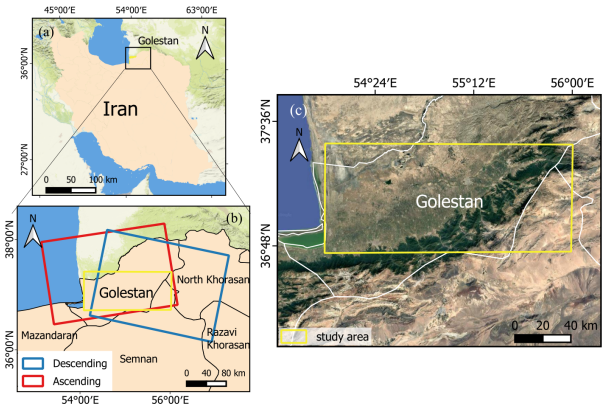

Figure 1. Location of Golestan Province.

Golestan Province is in northeastern Iran, near the Caspian Sea and the border with Turkmenistan. It covers about 20,000 km² and includes both mountain areas in the south and flat plains in the north. The climate is humid in the north and semi-arid inland. The average annual rainfall in the Province is approximately 454 mm mostly in winter, which is nearly twice the national average (Abdollahipour et al., 2021). Golestan is one of Iran’s main agricultural regions. Major crops include wheat, barley, rice, cotton, and oilseeds. Farming is supported by irrigation, and vegetation changes throughout the year.

We used Sentinel-1 single-look complex (SLC) data acquired from 2014 to 2024 for Golestan Province. Both ascending and descending orbits were utilized, specifically ascending path 057 and descending path 064, to provide complementary viewing geometries for surface deformation monitoring.

To analyze the seasonal climatic influence on ground deformation, we used temperature and precipitation datasets. The MOD11A1 V6.1 product (Wan et al., 2021) provides daily land surface temperature (LST) and emissivity at 1 km resolution, with both daytime and nighttime observations. For precipitation, we used Climate Hazards Center InfraRed Precipitation with Station data (CHIRPS)(Funk et al., 2015), a long-term quasi-global rainfall product that combines 0.05° resolution satellite data with ground station observations to generate high quality gridded time series suitable for trend analysis and drought monitoring. Both datasets were accessed and processed using Google Earth Engine (Gorelick et al., 2017), a cloud-based platform that facilitates efficient analysis of large geospatial datasets by providing scalable computing resources.

3. Methodology

3.1 Principle of SBAS-InSAR

In the SBAS-InSAR technique, all SAR images are coregistered and resampled to one of the images considered as the reference image. By imposing constraints on both temporal and spatial baselines, M differential interferograms are then generated between the resampled images acquired over the same area at epochs $(t_0, t_1, \ldots, t_N)$ (Berardino et al., 2003; Lanari et al., 2004). After removing the flat-earth and topographic phases and applying spatial phase unwrapping, these interferograms form a stack of unwrapped interferometric phases. The unwrapped interferometric phase is mainly composed of the deformation signal, atmospheric delays, residual topography, and noise (Hanssen, 2001). After removing the residual topographic component, SBAS-InSAR focuses on inverting the remaining phase to retrieve the deformation time-series. Mathematically, the inversion problem can be formulated as a system of M linear equations that link the interferometric phases to the unknown phase history vector (Berardino et al., 2003):

$$\boldsymbol{\Delta\phi} = \mathbf{A}\boldsymbol{\phi} + \boldsymbol{\epsilon}, \tag{1}$$

where $\boldsymbol{\Delta\phi} = [\Delta\phi_1, \Delta\phi_2, \ldots, \Delta\phi_M]^T$ is the $M \times 1$ vector of observed interferometric phases, $\boldsymbol{\phi} = [\phi_1, \phi_2, \ldots, \phi_N]^T$ is the unknown raw phase time-series relative to the reference acquisition t_0, $\mathbf{A}$ is the $M \times N$ design matrix determined by the interferogram network (each row contains -1 for the reference acquisition, $+1$ for the secondary acquisition, and zeros elsewhere), and $\boldsymbol{\epsilon}$ denotes the residual error vector capturing noise and unmodeled effects. If the interferogram network is fully connected and $\mathbf{A}$ has full rank, the system in Eq. (1) can be

solved using a weighted least-squares inversion:

$$\hat{\phi} = \left(\mathbf{A}^T\mathbf{W}\mathbf{A}\right)^{-1}\mathbf{A}^T\mathbf{W}\Delta\phi, \quad (2)$$

where $\mathbf{W}$ is an $M \times M$ diagonal weight matrix reflecting interferogram quality, and $\hat{\phi}$ is the estimated phase history. In cases where the interferogram network consists of multiple disconnected subsets, singular value decomposition (SVD) with a minimum-norm constraint is employed to obtain a unique and stable solution. This framework allows SBAS-InSAR to effectively recover the time-series deformation of coherent scatterers from a redundant set of interferometric measurements (Li et al., 2022).

3.2 Comparative Methodological Framework

Land deformation in Golestan Province from 2014 to 2024 was calculated by three SBAS-based time-series analysis packages, MintPy, LiCSBAS, and SARvey. Although they share the same theoretical principle, their workflows differ in several aspects. As for the input, we used interferograms and unwrapped phases generated by the Alaska Satellite Facility’s HyP3 (Hogenson et al., 2016) system for MintPy. HyP3 removes the topographic phase using the Copernicus GLO-30 Public DEM (European Space Agency, 2021) and applies snaphu (Chen and Zebker, 2002) for unwrapping. We used interferometric products from the LiCSAR (Lazeckỳ et al., 2020) system for LiCSBAS, which is tailored for large-scale Sentinel-1 processing and provides unwrapped interferograms and coherence estimates. Different from HyP3, LICSAR using the Shuttle Radar Topography Mission (SRTM) DEM (Farr et al., 2007) to remove the topographic phase. For SARvey, we processed the data with GAMMA, including coregistration and flat and topographic phase removal, while phase unwrapping was performed in SARvey using PUMA (Bioucas-Dias and Valadao, 2007) algorithm. In the time-series inversion step, MintPy, LiCSBAS, and SARvey use weighted least squares, NSBAS approach with temporal constraints and least squares method respectively. The study area lies in a mid-latitude region where ionospheric effects are generally negligible for C-band SAR observations, and the terrain is relatively smooth except for mountainous areas in the south, which limits topography-correlated tropospheric delays. Atmospheric artifacts were mitigated during the time-series processing, where the height correlation method was applied in MintPy and atmospheric phase screens were estimated in LiCSBAS and SARvey to reduce spatially correlated atmospheric noise. To ensure comparability across the three approaches, we applied the same multilooking factor of 4 in azimuth and 20 in range, considering the large spatial coverage of the study area.

4. Results and Discussion

4.1 Comparison of Mean Velocity

To evaluate the performance of different SBAS-InSAR based methods, we first examined the deformation results obtained from each processing chain. All three frameworks (MintPy, LiCSBAS, and SARvey) clearly indicate significant land subsidence in Golestan Province, primarily concentrated in the Gorgan Plain. The deformation follows a northeast–southwest elliptical pattern, with the magnitude gradually decreasing from the center toward the margins. Across all methods, the maximum line-of-sight (LOS) deformation rate reaches approximately 13 cm/year, confirming the presence of severe and spatially consistent subsidence that is likely associated with intensive groundwater extraction and agricultural activities.

Following this, a comparison was conducted against previous studies to further evaluate the performance of these methods. Specifically, we compared the average annual LOS deformation rates from our results (2014–2024) with those reported by Haghighi and Motagh (2024a), who applied SBAS-InSAR to the same region between 2014 and 2020 using Sentinel-1 data. As shown in Figure 2, all three processing methods yielded deformation patterns that are in strong agreement, particularly in the location and extent of the main subsiding areas as well as in the magnitude of the estimated subsidence, consistent with previous studies. This confirms not only the presence of significant

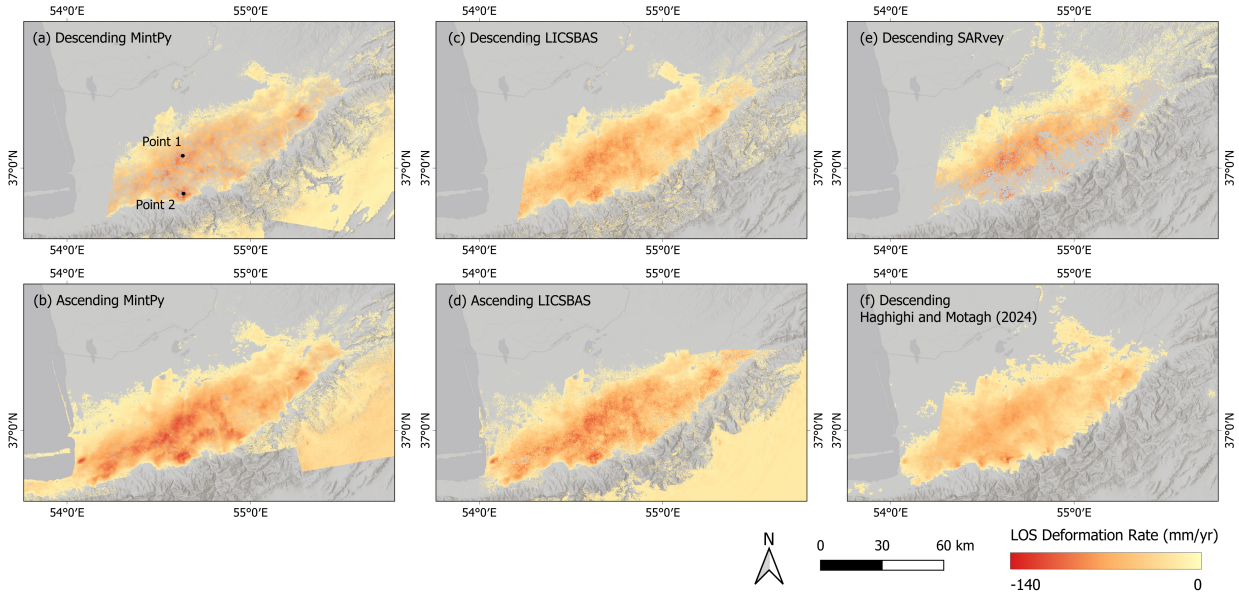

Figure 2. Comparison of Different LOS Deformation Rate Maps. Red and yellow areas represent the main deformation zones, where red indicates higher average annual deformation rates.

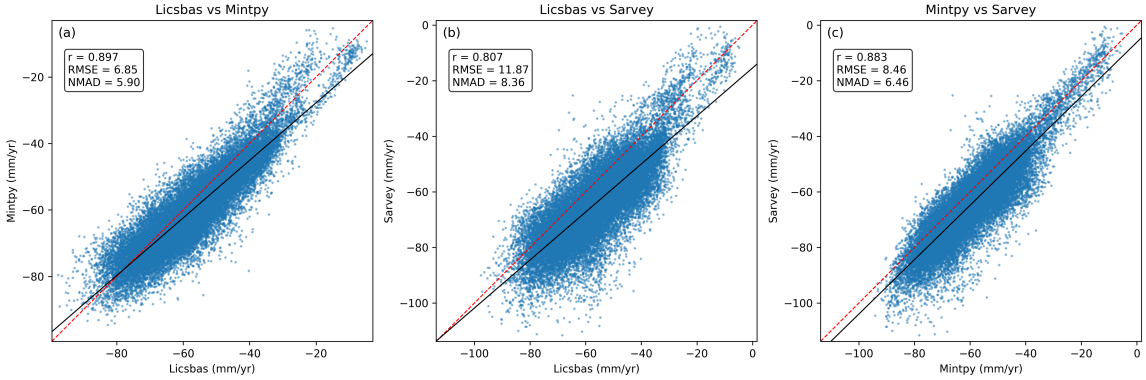

Figure 3. Pairwise scatter plots comparing LOS deformation rates derived from MintPy, LiCSBAS, and SARvey for the descending Sentinel-1 track. The red dashed lines represent the 1:1 reference, and the black solid lines show the best-fit regressions.

land subsidence in Golestan Province but also the reliability of SBAS-based methods even in areas with moderate coherence challenges.

SARvey provides a lower density of measurement points in low-coherence areas due to its two-step procedure for coherent pixel selection and phase unwrapping. This ensures that only reliable deformation estimates are retained. The reduction in coverage primarily affects vegetated or irrigated zones, where coherence is typically low. Nevertheless, SARvey still produces deformation patterns that are consistent with the other methods in areas of strong subsidence. MintPy and LiCSBAS retain more deformation pixels, which helps reveal finer details in the subsiding area. Among them, MintPy produces smoother deformation results.

To further evaluate the consistency among the three SBAS-InSAR frameworks, pairwise scatter plots of the descending-track LOS deformation rates were generated in Figure 3. Each scatter plot compares two processing chains and provides the corresponding Pearson correlation coefficient (r), together with the root mean square error (RMSE) and the normalized median absolute deviation (NMAD). The results show strong positive correlations among all frameworks, with r = 0.89 for LiCSBAS–MintPy, r = 0.88 for MintPy–SARvey, and r = 0.80 for LiCSBAS–SARvey. The RMSE values range from 6.85 to 11.87 mm/yr, while the NMAD values range from 5.90 to 8.36 mm/yr, indicating moderate differences among the pipelines but generally consistent deformation estimates. The relatively larger RMSE observed in the LiCSBAS–SARvey comparison likely reflects methodological differences between the frameworks, including variations in coherence masking, phase filtering, and pixel selection strategies. A clustering of points around deformation values of approximately 60 mm/yr can also be observed in the scatter plots, where SARvey tends to produce slightly larger subsidence rates than MintPy and LiCSBAS. This difference is likely related to variations in pixel selection and phase unwrapping strategies among the three processing frameworks. LiCSBAS uses the SRTM DEM and a relatively loose coherence threshold, allowing wider spatial coverage, whereas SARvey applies stricter pixel selection to ensure phase reliability. Despite these methodological variations, all three frameworks consistently show the same major subsiding zone in the Gorgan Plain and capture comparable deformation magnitudes. The quantitative results confirm that the SBAS-InSAR methods yield coherent and physically consistent deformation patterns even in low-coherence agricultural environments, highlighting their robustness under challenging conditions.

4.2 Line-of-Profile Analysis of Deformation Rates

To better assess the consistency among different SBAS-InSAR processing results, we performed a line-of-profile analysis across the primary subsiding area. As the main subsidence zone in Golestan exhibits a northeast–southwest elliptical shape, we selected two perpendicular profiles aligned with the major and minor axes of the ellipse (see Figures 4 and 5). These profiles allow for a detailed cross-sectional comparison of deformation rates and coherence behavior. In addition, the temporal coherence map, derived from the MintPy descending track processing results, is presented to illustrate the spatial distribution of phase stability. This information is essential for evaluating the reliability of the deformation estimates along the selected profiles.

Figure 4 (a) shows the spatial distribution of temporal coherence along the two selected profiles. Areas in red represent lower coherence values. It is evident that the southern mountainous region exhibits very low coherence due to dense vegetation cover. The main subsidence zone, located north of the mountains, also shows moderate-to-low coherence, although some urban surfaces remain identifiable as patches of consistently high coherence within the area. In Figure 4 (b), the deformation rates along the profile 1 are plotted for all available methods. Overall, the velocity curves from MintPy, LiCSBAS, and SARvey demonstrate strong agreement in both trend and location of maximum subsidence. Despite some fluctuations, most notably in the LiCSBAS results, all methods capture the same general deformation pattern. Compared with the 2014 to 2020 results from Haghighi and Motagh (2024a) (shown as the yellow curve), our results indicate a more pronounced rate of deformation from 2014 to 2024. This suggests that the deformation in the region has continued or even intensified over the period from 2020 to 2024. Figure 4 (c) presents the coherence values sampled along the profile 1. A clear decreasing trend is observed from north to south, consistent with increasing vegetation and topographic complexity. This coherence gradient helps explain the substantial loss of SARvey data in the southern section of the velocity map, as seen in Figure 2.

Figure 5 illustrates the deformation rate profiles and coherence values along the direction shown in Figure 4 (a) Profile 2, which corresponds to the major axis of the elliptical subsidence pattern. As shown in Figure 5 (a), the results derived from different SBAS-InSAR pipelines remain highly consistent along this

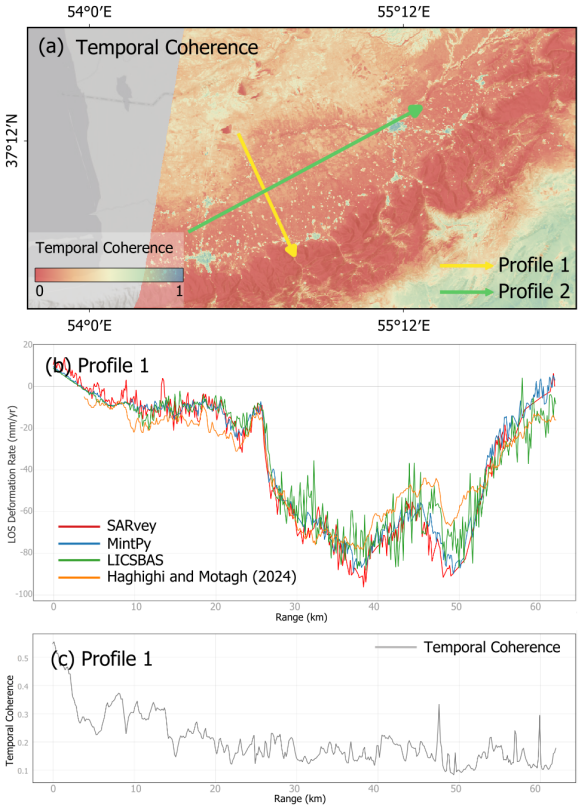

Figure 4. Profile Analysis. (a) Temporal coherence map from MintPy, red means low coherence. (b) Deformation rates along the minor axis profile 1. (c) Profile 1 of coherence values.

direction. All methods capture similar deformation trends and peak locations, indicating reliable agreement across processing approaches. Similar to Profile 1, Profile 2 also exhibits a more pronounced variation in deformation rates in our 2014–2024 results compared to the 2014–2020 results from Haghighi and Motagh (2024a), suggesting that deformation in this area has persisted or even accelerated in recent years. Figure 5 (b) shows the coherence values along the profile 2. Unlike the profile 1, coherence along this direction remains relatively stable, with no significant variation. This uniform coherence distribution likely contributes to the more complete and consistent retrieval of deformation across all methods in this section.

4.3 Time-Series Displacement

Compared to mean deformation rates, time-series displacement data provide a more detailed view of subsidence dynamics and are essential for understanding the temporal behavior of ground motion. As shown in Figure 6, we selected two points located within areas of severe subsidence to compare the deformation time-series derived from the three processing methods. These points were chosen in relatively stable locations to ensure that all methods yielded valid results at the same positions. Their locations are indicated in Figure 2 . Figures 6 (a-b) show the ground truth of the selected points. The first point is situated on a standalone building surrounded by agricultural land, while the second lies at the edge of a small town. Both locations exhibit good temporal coherence and stable scattering properties.

Figures 6 (c-d) present the time-series displacement curves at these two points, as obtained from MintPy, LiCSBAS, and

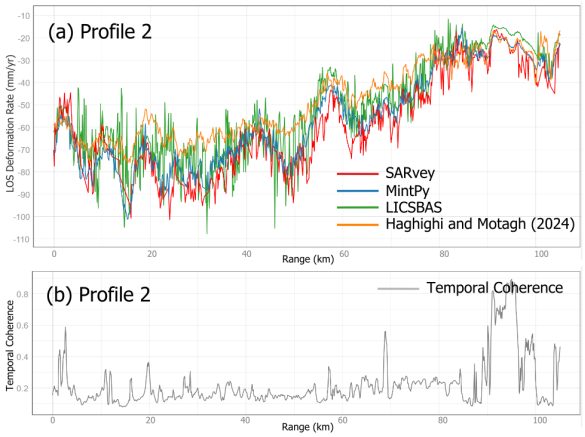

Figure 5. Profile Analysis Along the Major Axis of the Subsiding Zone.

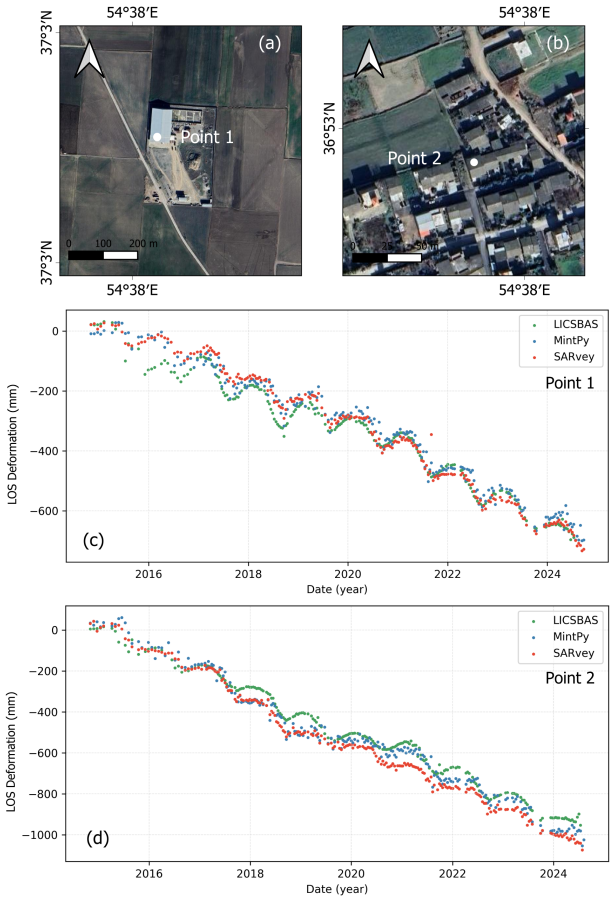

Figure 6. Time-Series Displacement Analysis at Two Selected Points. (a-b) Ground truth of the selected points, maps data: Google, Airbus. (c-d) Displacement time-series derived from LiCSBAS, MintPy, and SARvey for the two points.

SARvey. All three methods capture a consistent long-term subsidence trend, accompanied by clearly defined seasonal fluctuations. Each year, the displacement shows a modest uplift during winter months, followed by pronounced subsidence during summer. This pattern is likely related to seasonal groundwater use and recharge cycles in the region. While minor variations

This contribution has been peer-reviewed. The double-blind peer-review was conducted on the basis of the full paper.
https://doi.org/10.5194/isprs-annals-XI-3-2026-433-2026 | © Author(s) 2026. CC BY 4.0 License.

exist between the methods, the overall deformation trajectories remain closely aligned, without significant bias. Notably, both points show a temporary slowdown in subsidence between 2019 and 2020, which is more pronounced at Point 2. After 2021, the rate of subsidence increases again, indicating renewed or intensified deformation activity.

4.4 Temperature and Precipitation

The seasonal subsidence pattern observed in Golestan Province appears to be strongly correlated with local variations in surface temperature and precipitation. To investigate this relationship, we used MODIS MOD11A1 V6.1 land surface temperature (LST) data and CHIRPS daily precipitation data to examine the temporal correspondence between climate variables and surface deformation. To investigate this relationship, we first examined the temporal relationship between temperature and precipitation (Figure 7), which reflects the regional hydroclimatic seasonality. The results show that periods of high temperature generally coincide with reduced rainfall, indicating drier conditions and increased irrigation demand.

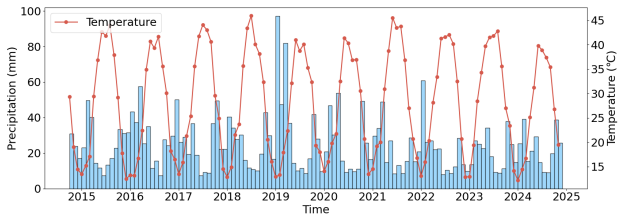

Figure 7. Relationship Between Surface Temperature and Precipitation

To isolate the seasonal component of the deformation signal, we removed the long-term linear trend from the displacement time-series at the selected points. This residual component highlights short-term fluctuations that can be linked to seasonal environmental drivers. Figure 8 illustrates the relationship between precipitation and deformation residuals. Golestan receives most of its annual rainfall during the winter season. This coincides with the uplift phases observed in the residual deformation signals. The timing suggests that increased winter precipitation contributes to shallow groundwater recharge and reduces the need for groundwater extraction for irrigation, thereby mitigating subsidence.

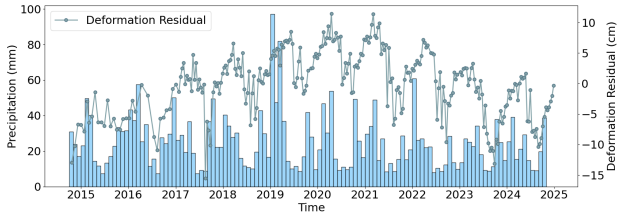

Figure 8. Relationship Between Precipitation and Seasonal Deformation Residuals

These observations support the hypothesis that seasonal deformation in Golestan is closely linked to hydroclimatic variability. Periods with high temperature and low precipitation promote subsidence. In contrast, cooler and wetter conditions favor aquifer recharge and ground uplift.

5. Conclusion

This study evaluated the performance of three SBAS-InSAR processing pipelines: MintPy, LiCSBAS, and SARvey. The assessment focused on their ability to monitor land subsidence in Golestan Province, Iran, a region characterized by intensive agriculture and low coherence conditions. Despite differences in their processing strategies, all three methods revealed consistent subsidence patterns, with Pearson correlation coefficients ranging from 0.80 to 0.89, and maximum annual deformation rates reaching approximately 13 cm/year, primarily concentrated in the Gorgan Plain.

The cross-section profiles showed that the results from the three methods matched well, with only small differences, especially in the LiCSBAS output. Time-series from selected stable points also showed good agreement and revealed clear seasonal patterns characterized by winter uplift and summer subsidence. Correlation analysis with surface temperature and precipitation confirmed that deformation residuals were strongly influenced by groundwater fluctuations driven by hydroclimatic conditions. Although SARvey produced fewer measurement points in low-coherence areas, likely related to its two-step unwrapping strategy. Its results remained reliable in high deformation zones. MintPy and LiCSBAS maintained broader spatial coverage, with MintPy producing smoother displacement fields.

Although ground-based validation data are not available in the study area, the reliability of the results is supported by the strong consistency among the three independent SBAS-InSAR frameworks and by the physically meaningful seasonal deformation patterns observed in the time-series. In addition, the spatial distribution of the identified subsidence zone agrees with previously reported deformation patterns in the region.

Overall, this study highlights the applicability of SBAS-InSAR methods in low-coherence environments and underscores the importance of incorporating climatic data for interpreting seasonal deformation. Future work could further investigate the sensitivity of deformation estimates to processing parameters and explore strategies to mitigate decorrelation and phase errors in intensively cultivated regions.

References

Abdollahipour, A., Ahmadi, H., Aminnejad, B., 2021. Evaluating the reconstruction method of satellite-based monthly precipitation over Golestan province, Northern Iran. *Acta Geophysica*, 69(6), 2305–2323.

Bawden, G. W., Thatcher, W., Stein, R. S., Hudnut, K. W., Peltzer, G., 2001. Tectonic contraction across Los Angeles after removal of groundwater pumping effects. *Nature*, 412(6849), 812–815.

Berardino, P., Fornaro, G., Lanari, R., Sansosti, E., 2003. A new algorithm for surface deformation monitoring based on small baseline differential SAR interferograms. *IEEE Transactions on geoscience and remote sensing*, 40(11), 2375–2383.

Bioucas-Dias, J. M., Valadao, G., 2007. Phase unwrapping via graph cuts. *IEEE Transactions on Image processing*, 16(3), 698–709.

Bürgmann, R., Rosen, P. A., Fielding, E. J., 2000. Synthetic aperture radar interferometry to measure Earth’s surface topography and its deformation. *Annual review of earth and planetary sciences*, 28(1), 169–209.

Chen, C. W., Zebker, H. A., 2002. Phase unwrapping for large SAR interferograms: Statistical segmentation and generalized network models. *IEEE Transactions on Geoscience and Remote Sensing*, 40(8), 1709–1719.

European Space Agency, 2021. Copernicus dem glo-30 public. European Space Agency. Data set.

Farr, T. G., Rosen, P. A., Caro, E., Crippen, R., Duren, R., Hensley, S., Kobrick, M., Paller, M., Rodriguez, E., Roth, L. et al., 2007. The shuttle radar topography mission. *Reviews of geophysics*, 45(2).

Faunt, C. C., Sneed, M., Traum, J., Brandt, J. T., 2016. Water availability and land subsidence in the Central Valley, California, USA. *Hydrogeology Journal*, 24(3), 675–684.

Ferretti, A., Prati, C., Rocca, F., 2002. Permanent scatterers in SAR interferometry. *IEEE Transactions on geoscience and remote sensing*, 39(1), 8–20.

Funk, C., Peterson, P., Landsfeld, M., Pedreros, D., Verdin, J., Shukla, S., Husak, G., Rowland, J., Harrison, L., Hoell, A. et al., 2015. The climate hazards infrared precipitation with stations—a new environmental record for monitoring extremes. *Scientific data*, 2(1), 1–21.

Gabriel, A. K., Goldstein, R. M., Zebker, H. A., 1989. Mapping small elevation changes over large areas: Differential radar interferometry. *Journal of Geophysical Research: Solid Earth*, 94(B7), 9183–9191.

Gorelick, N., Hancher, M., Dixon, M., Ilyushchenko, S., Thau, D., Moore, R., 2017. Google Earth Engine: Planetary-scale geospatial analysis for everyone. *Remote sensing of Environment*, 202, 18–27.

Haghighi, M. H., Motagh, M., 2024a. Land subsidence in iran estimated from a nationwide insar analysis of sentinel-1 observations (2014–2020).

Haghighi, M. H., Motagh, M., 2024b. Uncovering the impacts of depleting aquifers: A remote sensing analysis of land subsidence in Iran. *Science Advances*, 10. https://api.semanticscholar.org/CorpusID:269715441.

Hanssen, R. F., 2001. *Radar interferometry: data interpretation and error analysis*. Springer.

Hogenson, K., Arko, S. A., Buechler, B., Hogenson, R., Herrmann, J., Geiger, A., 2016. Hybrid pluggable processing pipeline (hyp3): A cloud-based infrastructure for generic processing of sar data. *Agu fall meeting abstracts*, 2016, IN21B–1740.

Lanari, R., Mora, O., Manunta, M., Mallorquí, J. J., Berardino, P., Sansosti, E., 2004. A small-baseline approach for investigating deformations on full-resolution differential SAR interferograms. *IEEE transactions on geoscience and remote sensing*, 42(7), 1377–1386.

Lazeckỳ, M., Spaans, K., González, P. J., Maghsoudi, Y., Morishita, Y., Albino, F., Elliott, J., Greenall, N., Hatton, E., Hooper, A. et al., 2020. LiCSAR: An automatic InSAR tool for measuring and monitoring tectonic and volcanic activity. *Remote Sensing*, 12(15), 2430.

Li, S., Xu, W., Li, Z., 2022. Review of the SBAS InSAR Time-series algorithms, applications, and challenges. *Geodesy and Geodynamics*, 13(2), 114–126.

Maghrebi, M., Noori, R., Partani, S., Araghi, A., Barati, R., Farnoush, H., Haghighi, A. T., 2021. Iran’s Groundwater Hydrochemistry. *Earth and Space Science*, 8. https://api.semanticscholar.org/CorpusID:237827358.

Mahmoudpour, M., Khamehchiyan, M., Nikudel, M. R., Ghassemi, M. R., 2016. Numerical simulation and prediction of regional land subsidence caused by groundwater exploitation in the southwest plain of Tehran, Iran. *Engineering Geology*, 201, 6–28.

Massonnet, D., Rossi, M., Carmona, C., Adragna, F., Peltzer, G., Feigl, K., Rabaute, T., 1993. The displacement field of the Landers earthquake mapped by radar interferometry. *nature*, 364(6433), 138–142.

Mohebbi Tafreshi, G., Nakhaei, M., Lak, R., 2021. Land subsidence risk assessment using GIS fuzzy logic spatial modeling in Varamin aquifer, Iran. *GeoJournal*, 86(3), 1203–1223.

Morishita, Y., Lazecky, M., Wright, T. J., Weiss, J. R., Elliott, J. R., Hooper, A., 2020. LiCSBAS: An open-source InSAR time series analysis package integrated with the LiCSAR automated Sentinel-1 InSAR processor. *Remote Sensing*, 12(3), 424.

Motagh, M., Shamshiri, R., Haghighi, M. H., Wetzel, H.-U., Akbari, B., Nahavandchi, H., Roessner, S., Arabi, S., 2017. Quantifying groundwater exploitation induced subsidence in the Rafsanjan plain, southeastern Iran, using InSAR time-series and in situ measurements. *Engineering Geology*, 218, 134-151. https://api.semanticscholar.org/CorpusID:133554972.

Osmanoğlu, B., Dixon, T. H., Wdowinski, S., Cabral-Cano, E., Jiang, Y., 2011. Mexico City subsidence observed with persistent scatterer InSAR. *International Journal of Applied Earth Observation and Geoinformation*, 13(1), 1–12.

Payne, J. A., Watson, A., Maghsoudi, Y., Ebmeier, S., Rigby, R., Lazeckỳ, M., Thomas, M., Elliott, J., 2025. Widespread extent of irrecoverable aquifer depletion revealed by country-wide analysis of land surface subsidence hazard in Iran. *Journal of Geophysical Research: Solid Earth*, 130(9), e2024JB030367.

Piter, A., Haghshenas Haghighi, M., Motagh, M., 2024. Challenges and Opportunities of Sentinel-1 InSAR for Transport Infrastructure Monitoring. *PFG–Journal of Photogrammetry, Remote Sensing and Geoinformation Science*, 92(5), 609–627.

Takagi, H., Esteban, M., Mikami, T., Pratama, M. B., Valenzuela, V. P. B., Avelino, J. E., 2021. People’s perception of land subsidence, floods, and their connection: A note based on recent surveys in a sinking coastal community in Jakarta. *Ocean & Coastal Management*, 211, 105753.

Tarchi, D., Casagli, N., Fanti, R., Leva, D. D., Luzi, G., Pasuto, A., Pieraccini, M., Silvano, S., 2003. Landslide monitoring by using ground-based SAR interferometry: an example of application to the Tessina landslide in Italy. *Engineering geology*, 68(1-2), 15–30.

Wan, Z., Hook, S., Hulley, G., 2021. Modis/terra land surface temperature/emissivity daily l3 global 1 km sin grid v061. Accessed: 29 Oct 2025.

Yunjun, Z., Fattahi, H., Amelung, F., 2019. Small baseline InSAR time series analysis: Unwrapping error correction and noise reduction. *Computers & Geosciences*, 133, 104331.

Zebker, H. A., Goldstein, R. M., 1986. Topographic mapping from interferometric synthetic aperture radar observations. *Journal of Geophysical Research: Solid Earth*, 91(B5), 4993–4999.

Zebker, H., Villasenor, J. et al., 1992. Decorrelation in interferometric radar echoes. *IEEE Transactions on geoscience and remote sensing*, 30(5), 950–959.